RESEARCH ARTICLE
PLANETARY SCIENCES

Earth and Planetary Physics
4: 420–428, 2020
doi: 10.26464/epp2020045

A local Martian crustal field model: Targeting the candidate landing site of the 2020 Chinese Mars Rover

XinZhou Li[1,2], ZhaoJin Rong[1,2,3]*, JiaWei Gao[1,2], Yong Wei[1,2,3], Zhen Shi[1,2], Tao Yu[4], and WeiXing Wan[1,2,3]

[1]Key Laboratory of Earth and Planetary Physics, Institute of Geology and Geophysics, Chinese Academy of Sciences, Beijing 100029, China;

[2]College of Earth Science, University of Chinese Academy of Sciences, Beijing 100049, China;

[3]Beijing National Observatory of Space Environment, Institute of Geology and Geophysics, Chinese Academy of Sciences, Beijing 100029, China;

[4]China University of Geosciences, Wuhan 430074, China

Key Points:

- A joint Mars Global Explorer (MGS) and Mars Atmosphere and Volatile Evolution (MAVEN) data set was used to establish a local crustal field model
- To establish the model, we adopted equivalent source dipoles in three layers with different buried depths
- Our model shows less misfit compared with other global crustal field models

Citation: Li, X. Z., Rong, Z. J., Gao, J. W., Wei, Y., Shi, Z., Yu, T., and Wan, W. X. (2020). A local Martian crustal field model: Targeting the candidate landing site of the 2020 Chinese Mars Rover. *Earth Planet. Phys.*, *4*(4), 420–428. http://doi.org/10.26464/epp2020045

Abstract: Unlike Earth, Mars lacks a global dipolar magnetic field but is dominated by patches of a remnant crustal magnetic field. In 2021, the Chinese Mars Rover will land on the surface of Mars and measure the surface magnetic field along a moving path within the possible landing region of 20°W–50°W, 20°N–30°N. One scientific target of the Rover is to monitor the variation in surface remnant magnetic fields and reveal the source of the ionospheric current. An accurate local crustal field model is thus considered necessary as a field reference. Here we establish a local crust field model for the candidate landing site based on the joint magnetic field data set from Mars Global Explorer (MGS) and Mars Atmosphere and Volatile Evolution (MAVEN) data combined. The model is composed of 1,296 dipoles, which are set on three layers but at different buried depths. The application of the dipole model to the joint data set allowed us to calculate the optimal parameters of their dipoles. The calculated results demonstrate that our model has less fitting error than two other state-of-the art global crustal field models, which would indicate a more reasonable assessment of the surface crustal field from our model.

Keywords: Mars; remnant crustal field; crustal field model; dipole sources; Chinese Mars mission

1. Introduction

Since the discovery of a remnant crustal field during the Mars Global Explorer (MGS) mission (1996–2006; Acuña et al., 1998), studies associated with the Martian crustal field have bloomed, and a remnant field model is widely required in these studies (e.g., Němec et al., 2011; Ma YJ et al., 2014). At present, many global models of the Martian crustal magnetic field have been established (e.g., Purucker et al., 2000; Cain et al., 2003; Chiao et al., 2006; Langlais et al., 2004; Whaler and Purucker, 2005; Arkani-Hamed, 2007; Lillis et al., 2008; Morschhauser et al., 2014; Moore and Bloxham, 2017). However, most models have been established based only on measurements from the MGS at an altitude of about 400 km during its main scientific phase.

After the MGS mission ended, the Mars Atmosphere and Volatile Evolution (MAVEN) mission (Jakosky et al., 2015) became a second mission in which the magnetic field was measured directly with the magnetometer onboard. By combining the field measurements from the MGS and MAVEN, Langlais et al. (2019) recently developed a new global remnant field model.

Nonetheless, the values of the magnetic field extrapolated to the surface of Mars were quite different among these models. As shown in Figure 1, arbitrarily taking the location of 35°W, 25°N as an instance, we plotted the altitude profiles of field strength over this location from the models of Arkani-Hamed (2007), Cain et al. (2003), Morschhauser et al. (2014), and Langlais et al. (2019), respectively. The differences in the extrapolated field strengths at low altitudes from these models are quite evident.

Additionally, future Mars missions, particularly the Landers and Rovers, will carry a magnetometer to measure the magnetic field on the surface of Mars. For example, the recent InSight mission carried a magnetometer to measure the magnetic field of the Mars surface, which is beneficial for magnetic field-based studies of the Martian interior, ionosphere, and extent to which conditions in the solar wind affect the Martian surface environment

---

Correspondence to: Z. J. Rong, rongzhaojin@mail.iggcas.ac.cn
Received 03 MAR 2020; Accepted 27 APR 2020.

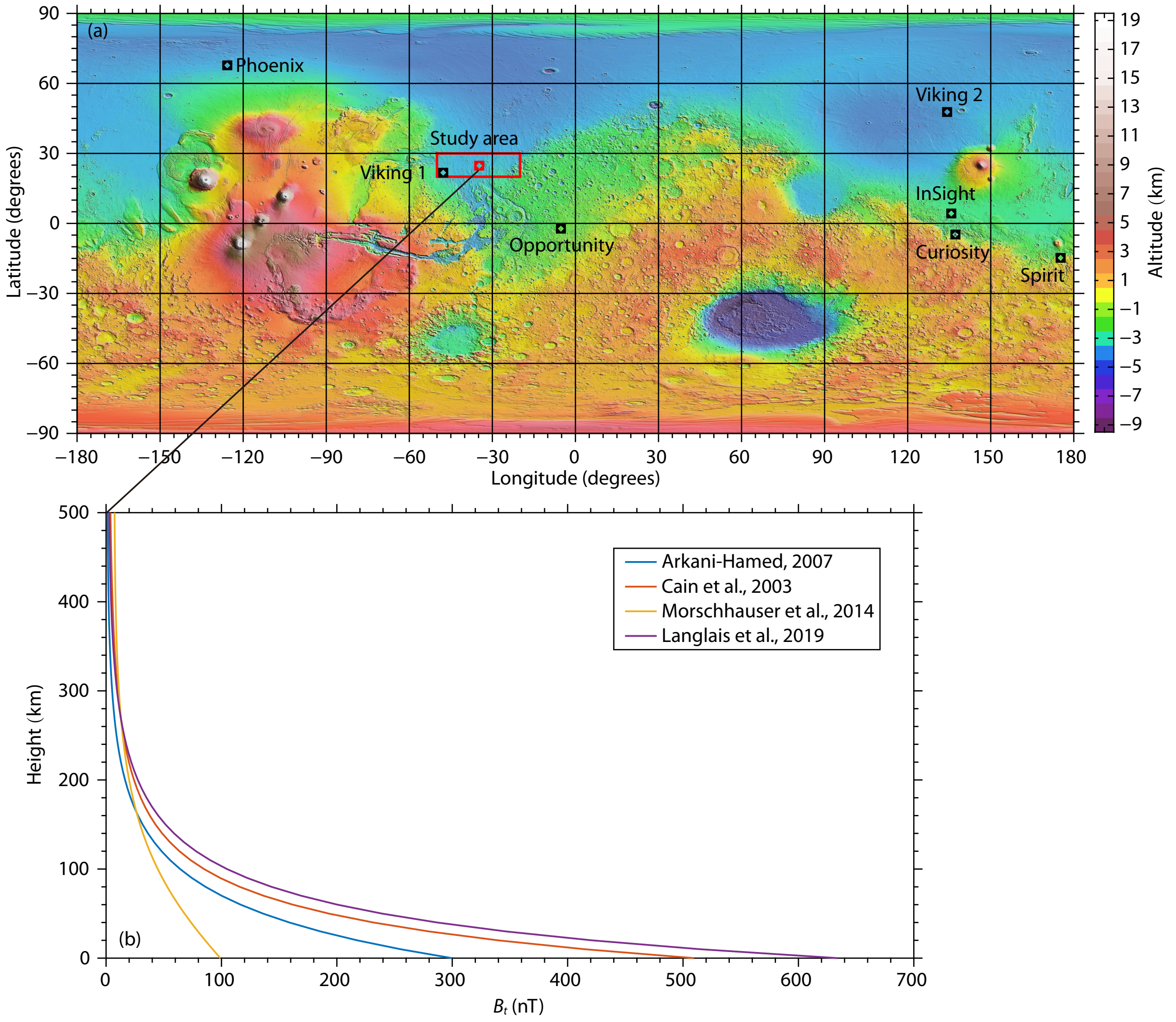

Figure 1. (a) Topographic map of Mars, on which the candidate landing region of the 2020 Chinese Mars Rover is marked as a red rectangle whose center (35°W, 25°N) is labeled by a red dot. (b) Height profiles of different models above the site of the red dot. B_t is the field strength.

(Johnson et al., 2019; Russell et al., 2019). Therefore, the regional models used to predict the surface remnant field are vital to future Mars missions. With the MGS data, Plattner and Simons (2015) constructed local models of the Martian South Polar Region. By combining the MGS and MAVEN data, Mittelholz et al. (2018a) developed a regional field model in the vicinity of the InSight landing site. Mittelholz et al. (2018b) also constructed a local field model to select the candidate landing site for the 2020 Mars mission (Mustard et al., 2013).

In 2020, China will launch its first Mars mission since the launch failure of the Yinghuo-1 probe in 2011 (Geng Y et al., 2018). This mission will include a rover carrying a magnetometer to measure the surface remnant field (Li CL et al., 2018; Zhao L et al., 2018). Its scientific goals include exploring the influence of the ionospheric current on the surface magnetic field (Wei Y et al., 2018) and the influence of the crustal field on the local atmospheric ion escape, as pointed out recently by MAVEN observations (Fan K et al., 2019). Thus, having an accurate preestimate of the surface field is vital for setting the magnetometer range onboard and deploying the other associated scientific plans.

Considering that the surface fields extrapolated from the present available global models are quite different, we were motivated to develop a new local crustal field model based on measurements from the MGS and MAVEN that would be particularly focused on the candidate landing region of the 2020 Chinese Mars Rover and would show less fitting error than that of other global models.

This paper is organized as follows. In Section 2, we introduce the data set used and the associated spacecraft. In Section 3, we present our approach to establishing the model. In Section 4, we compare the misfit of our model with two state-of-the art global models and calculate the extrapolated surface field by relying on this new model. In Section 5, we provide a summary and discussion.

2. Data Sets

2.1 Study Region and Spacecraft

As shown by the red rectangle in Figure 1a, the 2020 Chinese Mars Rover is scheduled to land within the region of 20°W–50°W, 20°N–30°N. To avoid model truncation at the area boundary, the region used for establishing the model was expanded to 17°W–53°W, 19°N–31°N in our study.

In this study, the magnetometer data sets of the MGS and MAVEN were combined for analysis. In the earlier aerobraking period and the science phasing orbits, the MGS had a large elliptical orbit and could dip down deeply to an altitude of about 100 km. The subsequent mapping orbit of the MGS became nearly circular, with an altitude that varied from 360 to 415 km for a long time (March 1999 to November 2006) (Albee et al., 2001). The data set available from the MGS magnetometer covers the period from 14 September 1997 to 2 November 2006.

The MAVEN mission was launched on 18 November 2013 and went into orbit around Mars on 21 September 2014. The MAVEN spacecraft was in an elliptical orbit for a period of 4.5 hours, with a periapsis altitude of about 150 km (with several campaigns down to ~125 km) and apoapsis of about 6,200 km. In other words, the MAVEN orbit had wider altitude coverage than that of the MGS to measure the remnant field (Connerney et al., 2015). The data set from the MAVEN magnetometer used in this study covers the period from 2 November 2014 to 31 January 2018.

2.2 Data Selection

To establish a reasonable remnant field model, one must try to minimize the disturbance from external field sources (i.e., magnetospheric currents and ionospheric currents) as much as possible. We adopted the following criteria to constrain the data set:

(1) To predict the surface field more accurately, more data points with a low altitude were required. To increase the proportion of low-altitude data points in the data set, we included more data points from the MAVEN at lower altitudes. Thus, we adopted a time resolution for the MAVEN data set of 1 sec and for the MGS data set of 1 min.

(2) Similar to previous global models (e.g. Purucker et al., 2000; Langlais et al., 2004), we selected only nightside data from the joint data set to minimize disturbance from the external magnetic field. Here, nightside is defined as when the solar zenith angle of the spacecraft is greater than 90°.

(3) Considering that the typical height of the ionopause is about 500 km (Han X et al., 2014; Han QQ et al., 2019), we further restricted the data set to altitudes below 500 km to minimize disturbance from the magnetospheric currents.

(4) Mittelholz et al. (2018a) found that the strength of the upstream interplanetary magnetic field (IMF) could be seen as a proxy to separated magnetically quiet and noisy data. They found that the magnetic measurement of one orbit could be seen in quiet time if it's upstream IMF strength was, on average, lower than 3.8 nT. Thus, from the remaining MAVEN data set, we retained only the orbits whose corresponding upstream IMF strength was, on average, lower than 3.8 nT (Mittelholz et al., 2018a). The average IMF was calculated by the 30-min average centered on the apoapsis time when the apoapsis of the MAVEN orbit was beyond the bow shock model (Trotignon et al., 2006). Because the MGS did not cross the bow shock during the mapping orbit period, we could not exert the IMF criteria to select the quiet time period for the MGS data set.

(5) To further lower the external field disturbance of the remaining MGS data set, we partitioned the spatial volume (longitude 17°W–53°W, latitude 19°N–31°N, height 350–450 km) into bins of 0.2° × 0.2° × 12.5 km (longitude × latitude × height). We retained only the bins that included at least 3 data points, and then chose the data point whose field strength was the bin median as the representative data point for that bin.

Following the above criteria, we finally collected 10,225 data points to constitute the MGS data set and 12,386 data points to constitute the MAVEN data set. The distributions of data points for the MGS and MAVEN are shown in Figure 2a and 2b, respectively, and the height profile of all points within the area (17°W–53°W, 19°N–31°N) is shown in Figure 2c. The data points of the MGS were clearly uniformly distributed in the latitude–longitude plane, but they had insufficient height coverage. In contrast, the MAVEN had a wider height coverage but inhomogeneous coverage in the latitude–longitude plane.

In this study, the planetocentric coordinate system was used. In this coordinate system, the *x*-axis points towards 0°E, the *y*-axis points toward 90°W, and the *z*-axis points toward the spin direction of Mars. At the same time, in the frame of the planetocentric coordinate system, the associated local spherical coordinates $\{\hat{r}, \hat{\theta}, \hat{\varphi}\}$ are defined, where $\hat{r}$ is radially outward, $\hat{\theta}$ is southward, and $\hat{\varphi}$ is eastward. For example, B_r, B_θ, and B_φ represent the outward, southward, and eastward components of the magnetic field, respectively.

3. Approach of the Model

Two general methods are available to build the Martian remnant field model. One is the spherical harmonic analysis method, which is done by solving the potential field directly with the boundary constraints by using the observations from the spacecraft (Cain et al., 2003; Arkani-Hamed, 2007; Morschhauser et al., 2014; Langlais et al., 2019). The other is the equivalent source dipoles (ESD) method. In contrast to the spherical harmonic analysis, the ESD fits the observed field with an assumed distribution of magnetic dipoles. The ESD was first applied to construct a model of the Earth's crustal field (e.g., Mayhew, 1979) and has since been successfully applied to build magnetic field models of the Moon (e.g., Purucker, 2008), Mercury (Oliveira et al., 2015), and Mars (e.g., Purucker et al., 2000; Langlais et al., 2004, 2019; Mittelholz et al., 2018a, b).

On the basis of the inferred average Martian crustal thickness of about 50 km (Zuber, 2001; Smith and Zuber, 2002), previous ESD models of the Martian crustal field have set the dipoles or magnetized layers to a depth of about 40 km (e.g. Purucker et al., 2000, Langlais et al., 2004, Mittelholz et al., 2018a, b). However, the study by Arkani-Hamed (2005) demonstrated that the same impacts that create craters can demagnetize the uppermost part of the crust (i.e., craters of diameters < 50 km can demagnetize the upper 10–20 km of the crust) and suggested that the magnetic source could be distributed mainly at depths of 55–45, 90–80, and 100–90 km beneath the Martian surface if hematite, magnetite,

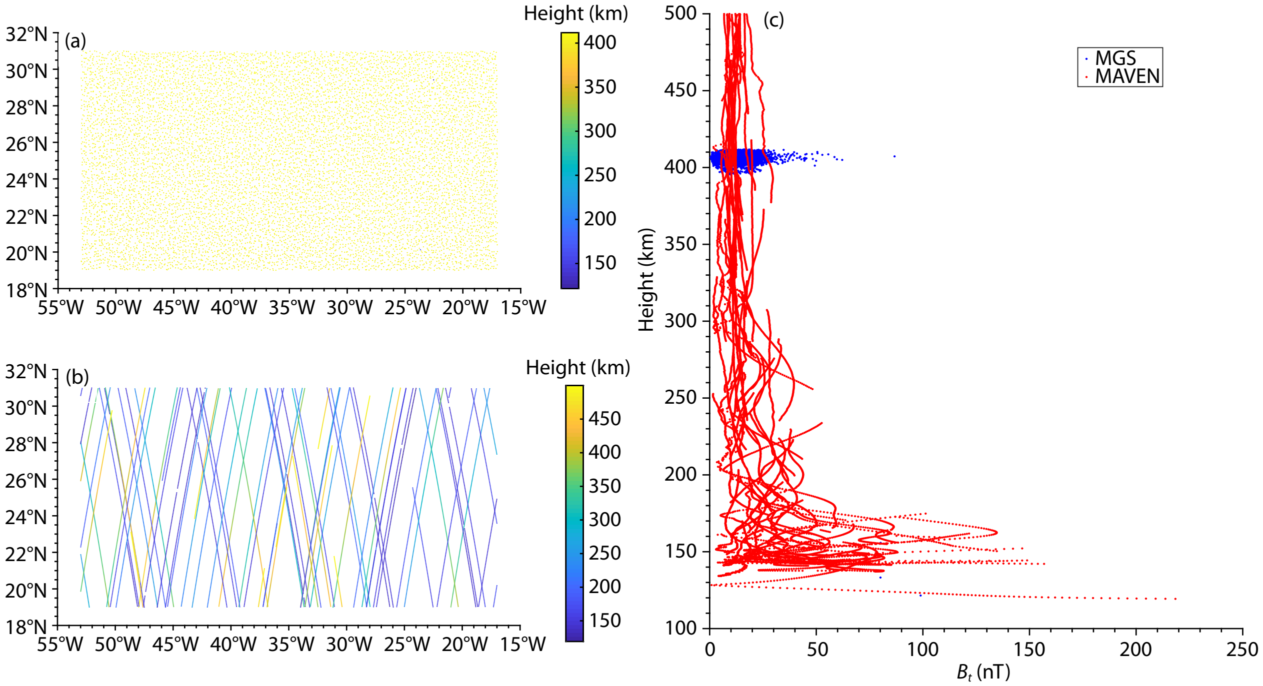

Figure 2. Distribution of data points from the (a) MGS and (b) MAVEN, respectively. The data points in both panels are colored according to their heights. (c) Height profile of the magnetic field strength for all the data points.

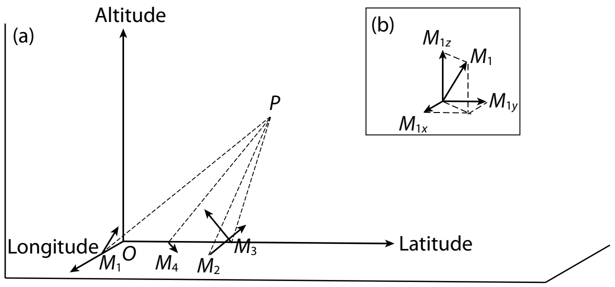

Figure 3. Schematic diagram showing the model approach. (a) A set of dipoles are placed in each layer, with random dipole directions. The magnetic field observed at point *P* is the sum of the contributions of all the dipoles. (b) Each dipole can be decomposed into three components along the direction of *x*, *y*, and *z*, respectively.

and pyrrhotite were the major magnetic carriers, respectively.

Considering the previous ESD models and the geochemical study of magnetic sources by Arkani-Hamed (2005), our study adopted the ESD method to establish a local field model in which the dipole sources were set on three layers with different burial depths, namely, 50, 85, and 95 km, respectively. The region of concern (17°W–53°W, 19°N–31°N) was partitioned into bins of 1° × 1° (longitude × latitude). We obtained 432 bins in each layer and 1,296 bins in total. At the center of each bin on each layer, a magnetic dipole ***M*** was set oriented along an arbitrary direction.

As sketched in Figure 3a, our task was to search for the optimal parameters of these dipoles, including their strengths and directions, on the three layers to best fit the joint data set. To facilitate this calculation, each dipole ***M*** was decomposed into three components, M_x, M_y, and M_z, pointing toward the *x*, *y*, and *z* axes, respectively (see Figure 3b). In other words, to invert the magnetic sources, we had to calculate the optimal 3,888 parameters for the dipole moments.

It is well-known that the magnetic field induced by the *i*th dipole with an arbitrary orientation is

$$\boldsymbol{B}_j = -\frac{\mu_0 \boldsymbol{M}_i}{4\pi r_{ji}^3} + \frac{3\mu_0\left(\boldsymbol{M}_i \cdot \boldsymbol{r}_{ji}\right)\boldsymbol{r}_{ji}}{4\pi r_{ji}^5}, \tag{1}$$

where $\boldsymbol{B}_j$ is the *j*th measured field vector induced by the dipole, $\boldsymbol{M}_i$ is the vector of the dipole moment, $\boldsymbol{r}_{ji}$ is the radial vector from the dipole to the measured data point, and μ_0 is the magnetic permeability; here, *j* is equal to 1, 2…*N*, where *N* is the number of sampled field vectors, and *i* is equal to 1, 2…*K*, where *K* is the total number of dipoles we set.

In Cartesian coordinates, the three respective components of a magnetic field induced by the *i*th dipole can be expanded via Equation (1) as follows:

$$\begin{cases} B_{jx} = -\dfrac{\mu_0 M_{ix}}{4\pi r_{ji}^3} + \dfrac{3\mu_0\left(\boldsymbol{M}_i \cdot \boldsymbol{r}_{ji}\right) r_{jix}}{4\pi r_{ji}^5}, \\ B_{jy} = -\dfrac{\mu_0 M_{iy}}{4\pi r_{ji}^3} + \dfrac{3\mu_0\left(\boldsymbol{M}_i \cdot \boldsymbol{r}_{ji}\right) r_{jiy}}{4\pi r_{ji}^5}, \\ B_{jz} = -\dfrac{\mu_0 M_{iz}}{4\pi r_{ji}^3} + \dfrac{3\mu_0\left(\boldsymbol{M}_i \cdot \boldsymbol{r}_{ji}\right) r_{jiz}}{4\pi r_{ji}^5}. \end{cases} \tag{2}$$

Equation (2) can be further rewritten as follows:

$$\begin{pmatrix} \boldsymbol{b}_x \\ \boldsymbol{b}_y \\ \boldsymbol{b}_z \end{pmatrix}_{3N\times 1} = \begin{pmatrix} G_{xx} & G_{xy} & G_{xz} \\ G_{yx} & G_{yy} & G_{yz} \\ G_{zx} & G_{zy} & G_{zz} \end{pmatrix}_{3N\times 3K} \begin{pmatrix} \boldsymbol{m}_x \\ \boldsymbol{m}_y \\ \boldsymbol{m}_z \end{pmatrix}_{3K\times 1}, \tag{3}$$

where $\boldsymbol{b}_x = \begin{pmatrix} B_{1x} \\ B_{2x} \\ \dots \\ B_{Nx} \end{pmatrix}$, $\boldsymbol{b}_y = \begin{pmatrix} B_{1y} \\ B_{2y} \\ \dots \\ B_{Ny} \end{pmatrix}$, $\boldsymbol{b}_z = \begin{pmatrix} B_{1z} \\ B_{2z} \\ \dots \\ B_{Nz} \end{pmatrix}$, $\boldsymbol{m}_x = \begin{pmatrix} M_{1x} \\ M_{2x} \\ \dots \\ M_{Kx} \end{pmatrix}$,

$\boldsymbol{m}_y = \begin{pmatrix} M_{1y} \\ M_{2y} \\ \dots \\ M_{Ky} \end{pmatrix}$, and $\boldsymbol{m}_z = \begin{pmatrix} M_{1z} \\ M_{2z} \\ \dots \\ M_{Kz} \end{pmatrix}$.

Variable $\boldsymbol{G}$ is a transform matrix of dimensions $3N \times 3K$. Each element of $\boldsymbol{G}$ is a matrix of dimensions $N \times K$, which can be written specifically as follows:

$$G_{xx} = \frac{\mu_0}{4\pi}\left(\frac{-1}{r_{NK}^3} + \frac{r_{NKx}^2}{r_{NK}^5}\right),\ G_{xy} = \frac{3\mu_0}{4\pi}\frac{r_{NKy}r_{NKx}}{r_{NK}^5},\ G_{xz} = \frac{3\mu_0}{4\pi}\frac{r_{NKz}r_{NKx}}{r_{NK}^5},$$

$$G_{yx} = \frac{3\mu_0}{4\pi}\frac{r_{NKx}r_{NKy}}{r_{NK}^5},\ G_{yy} = \frac{\mu_0}{4\pi}\left(\frac{-1}{r_{NK}^3} + \frac{r_{NKy}^2}{r_{NK}^5}\right),\ G_{yz} = \frac{3\mu_0}{4\pi}\frac{r_{NKz}r_{NKy}}{r_{NK}^5},$$

$$G_{zx} = \frac{3\mu_0}{4\pi}\frac{r_{NKx}r_{NKz}}{r_{NK}^5},\ G_{zy} = \frac{3\mu_0}{4\pi}\frac{r_{NKy}r_{NKz}}{r_{NK}^5},\ \text{and}\ G_{zz} = \frac{\mu_0}{4\pi}\left(\frac{-1}{r_{NK}^3} + \frac{r_{NKz}^2}{r_{NK}^5}\right).$$

With Equation (3), the basic equation for this model can be expressed simply as

$$\boldsymbol{b} = \boldsymbol{Gm} + \boldsymbol{v}, \tag{4}$$

where $\boldsymbol{b} = \begin{pmatrix} \boldsymbol{b}_x \\ \boldsymbol{b}_y \\ \boldsymbol{b}_z \end{pmatrix}$, $\boldsymbol{m} = \begin{pmatrix} \boldsymbol{m}_x \\ \boldsymbol{m}_y \\ \boldsymbol{m}_z \end{pmatrix}$,

$\boldsymbol{G}$ is a transform matrix that is a function of the relative distance between dipoles and observation points, and $\boldsymbol{v}$ is a vector of error. The least squares solution of Equation (4) can be derived as follows:

$$\boldsymbol{m} = \left(\boldsymbol{G}^{\mathrm{T}}\boldsymbol{G}\right)^{-1}\boldsymbol{G}^{\mathrm{T}}\boldsymbol{b}. \tag{5}$$

To solve Equation (5), we adopted the conjugate gradient method (Hestenes and Stiefel, 1952; Purucker et al., 1996) to numerically calculate $\boldsymbol{m}$ with the initial values (see the detailed algorithm in Appendix A).

As the number of iterations increases, the root mean square (RMS) should gradually decrease and converge. From Equation (5), the RMS after the kth iteration can be calculated as follows:

$$\sigma_k = \sqrt{\frac{\left(\boldsymbol{b} - \boldsymbol{Gm}_k\right)^{\mathrm{T}}\left(\boldsymbol{b} - \boldsymbol{Gm}_k\right)}{3N}}, \tag{6}$$

where the subscript k represents the kth iteration. Note that because all three field components are involved in the calculation, the denominator should be $3N$ instead of N. According to previous studies (Langlais et al., 2019), when the calculated σ_k satisfies

$$\Delta\sigma_k = \frac{\sigma_k - \sigma_{k-1}}{\sigma_k} < 0.5\%, \tag{7}$$

we terminate the calculation and return to the dipole parameters we searched for.

If we take $G_x = [G_{xx}\ G_{xy}\ G_{xz}]$, $G_y = [G_{yx}\ G_{yy}\ G_{yz}]$, and $G_z = [G_{zx}\ G_{zy}\ G_{zz}]$, the RMS after the kth iteration for the B_x, B_y, and B_z components can be written respectively as follows:

$$\sigma_{kx} = \sqrt{\frac{\left(\boldsymbol{b}_x - G_x\boldsymbol{m}_k\right)^{\mathrm{T}}\left(\boldsymbol{b}_x - G_x\boldsymbol{m}_k\right)}{N}}, \tag{8}$$

$$\sigma_{ky} = \sqrt{\frac{\left(\boldsymbol{b}_y - G_y\boldsymbol{m}_k\right)^{\mathrm{T}}\left(\boldsymbol{b}_y - G_y\boldsymbol{m}_k\right)}{N}}, \tag{9}$$

$$\sigma_{kz} = \sqrt{\frac{\left(\boldsymbol{b}_z - G_z\boldsymbol{m}_k\right)^{\mathrm{T}}\left(\boldsymbol{b}_z - G_z\boldsymbol{m}_k\right)}{N}}. \tag{10}$$

Accordingly, the RMS for the strength of the magnetic field can be written as follows:

$$\sigma_{kt} = \sqrt{\frac{\left(\boldsymbol{B}_t - \boldsymbol{b}_{tk}\right)^{\mathrm{T}}\left(\boldsymbol{B}_t - \boldsymbol{b}_{tk}\right)}{N}}, \tag{11}$$

where $\boldsymbol{B}_t = \sqrt{\boldsymbol{b}_x^2 + \boldsymbol{b}_y^2 + \boldsymbol{b}_z^2}$, $\boldsymbol{b}_{tk} = \sqrt{\left(G_x\boldsymbol{m}_k\right)^2 + \left(G_y\boldsymbol{m}_k\right)^2 + \left(G_z\boldsymbol{m}_k\right)^2}$.

However, to solve Equation (5) by least squares, multiple local minima could be in the space of the dipole parameters. The optimal dipole parameters we searched for would depend strongly on the set of initial values. There is no general way to overcome this difficulty in principle.

To check the consistency of the final outputs, we tried different sets of initial values. In our trial calculation, the initial values of the components M_x, M_y, and M_z of all the dipoles were set the same, as $\pm 10^{\alpha}$ A·m^2, where α is a variable from 0 to 16 with a step of 0.5.

In Figure 4a, on the basis of Equations (9) to (12), we show the final calculated RMS for B_x, B_y, B_z, and B_t, respectively, against the different sets of initial values. Obviously, the calculated RMS was rather stable when the initial value fell within the range of $\pm 10^{14}$ A·m^2, and we found that it stably required 18 iterations to terminate the calculation within this range (Figure 4b). We checked the output for the different sets of initial values and found that the values of M_x, M_y, and M_z we searched for were almost the same (not shown here).

We also checked the case when the initial values between M_x, M_y, and M_z were different and found that the outputs were still basically unchanged if the initial values fell in the range of $\pm 10^{14}$ A·m^2 (not shown here). Thus, to calculate the model parameters, we finally arbitrarily set the initial values for components M_x, M_y, and M_z as 1 A·m^2.

4. Results

The RMS for all the field components could be calculated based on Equations (6) to (11). The final output is tabulated in Table 1 and includes a comparison with two state-of-the art global models, namely, the models by Morschhauser et al. (2014) and Langlais et al. (2019), hereafter referred to as M14 and L19, respectively. Note that to calculate the RMS for M14 and L19, one needs to replace only the term $\boldsymbol{Gm}$ in Equations (8) to (11) by the magnetic field inferred from the models. As presented in Table 1, our model appeared to have significantly less misfit than either M14 or L19.

Figure 5 shows the extrapolated distributions of the radial field component, B_r, and field strength, B_t, on the Martian surface from our model compared with M14, and L19, respectively. We found that the overall distribution patterns of B_r and B_t were basically the same for the three models. The major difference, however, consisted of the fine characteristics in some locations. For example, near the location of 20°W, 30°N, our model predicted a stronger

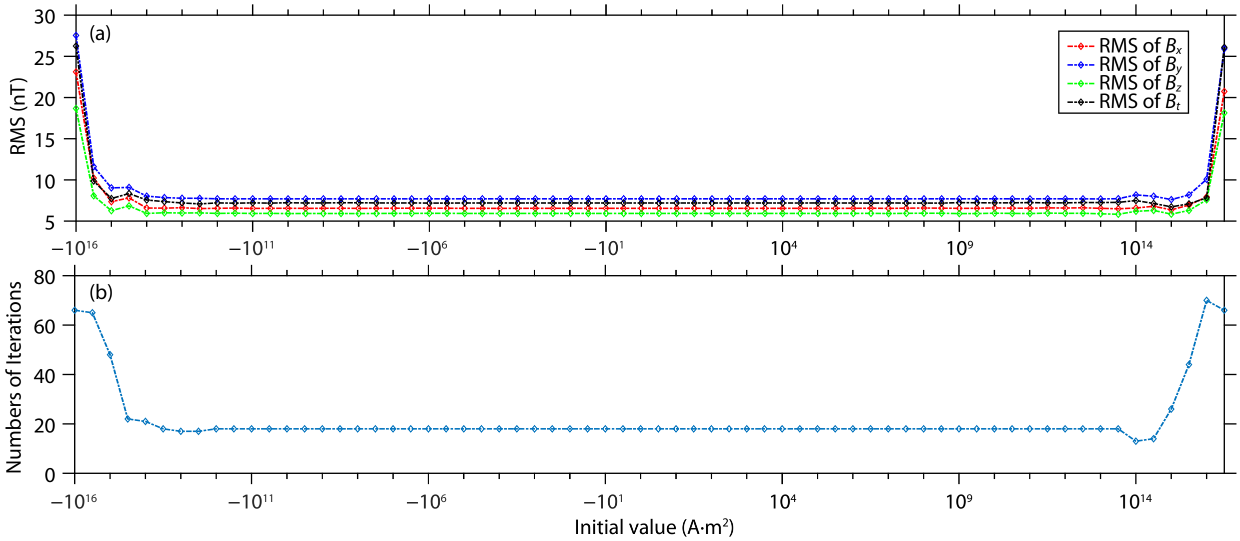

Figure 4. Dependence of the (a) final misfit and (b) number of iterations on the initial values of the dipole moments. The three components of the dipole moment were set the same, as 10^{α} A·m^2.

Table 1. Comparison of root mean squares (RMS) for our model with the models by Morschhauser et al. (2014; M14) and Langlais et al. (2019; L19).

	RMS σ (nT)		
	This study	M14	L19
B_x	6.590	10.250	9.052
B_y	7.671	10.026	9.886
B_z	5.839	8.052	7.533
B_r	6.792	9.665	9.075
B_θ	6.332	8.216	7.784
B_φ	7.080	10.464	9.668
B_t	7.311	9.967	9.635

field strength (~2,400 nT) than did either the M14 or L19 (~1,500 nT).

Figure 6a and 6b show the distribution of the strength and orientation of the dipoles at each layer, based on the inverted M_x, M_y, and M_z components for all the dipoles. At least two features can be observed in Figure 6. First, the dipole moment on the shallow layer is stronger, which could be the main source responsible for the surface field. Second, consistent with Figure 5, a stronger surface field corresponds to stronger dipoles in each layer.

5. Summary and Discussion

In this study, we developed a new local Martian crustal field model with the technique of equivalent magnetic dipoles by combining the magnetic field measurements of the MGS and MAVEN. Our model has an advantage over previous dipole models. In previous dipole models, the dipoles were set with the radial orientation on only one layer, at a depth of 40 km (e.g., Purucker et al., 2000; Langlais et al., 2004). In contrast, the dipoles in our model were set to be more relaxed, with arbitrary orientations on the three layers. The dipole parameters of our model were solved by least squares when applied to the joint data set. To guarantee the consistency of the dipole parameters we searched for, different trials of initial parameter values were conducted. The final dipole parameters yielded by this process demonstrated that our model had much lower fitting error in comparison with the two other state-of-the art global models. Thus, from our model, the field extrapolated to the Martian surface would be more reasonable than those from the previous global models.

The lower error of our model can easily be understood in that the local contributions could have been smoothed out in the global models. This is also why a local field model is required to infer the local surface field.

Comparison of our model with the global models suggests that the extrapolated surface field from our model could be more inhomogeneous and that the field strength in some locations could be much stronger than those predicted by the global models. Thus, we suggest that the magnetometer carried by the 2020 Chinese Rover should be designed with a wider range to measure the inhomogeneity of the surface field.

Several points about our model should be discussed and caution exercised:

(1) In principle, the misfit or RMS should decrease with an increase in the number of dipoles. A model with more dipoles could fit the data better; however, more dipoles would result in a greater expense of calculation time. Moreover, to maintain the solvability of Equation (5), the number of dipoles in the model should be less than the number of data points.

(2) One may argue that the initial value we chose could be unreasonable and that calculation could terminate at some local minima. To test this argument, we could use a field data set generated by L19 at the lower altitude to invert the dipole moments by our model, and the inverted dipole moments could be seen as more reasonable initial values to run our model again when subjected

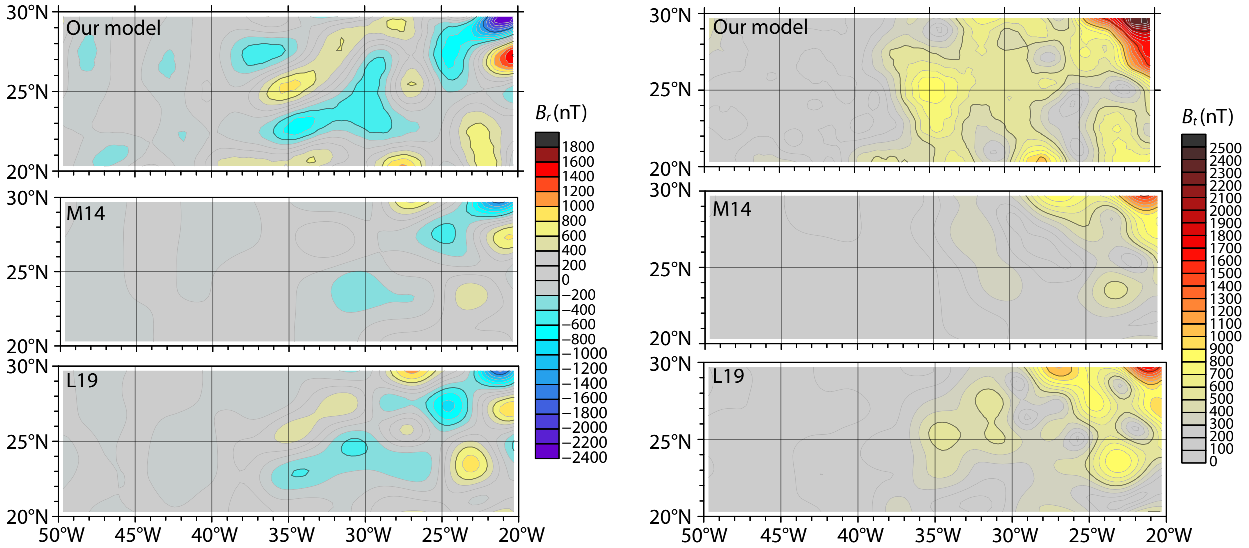

Figure 5. From top to bottom, panels show the extrapolated radial magnetic field (left column) and magnetic field strength (right column) on the surface of Mars from our model, the M14 (the model by Morschhauser et al., 2014) and the L19 (the model by Langlais et al., 2019), respectively.

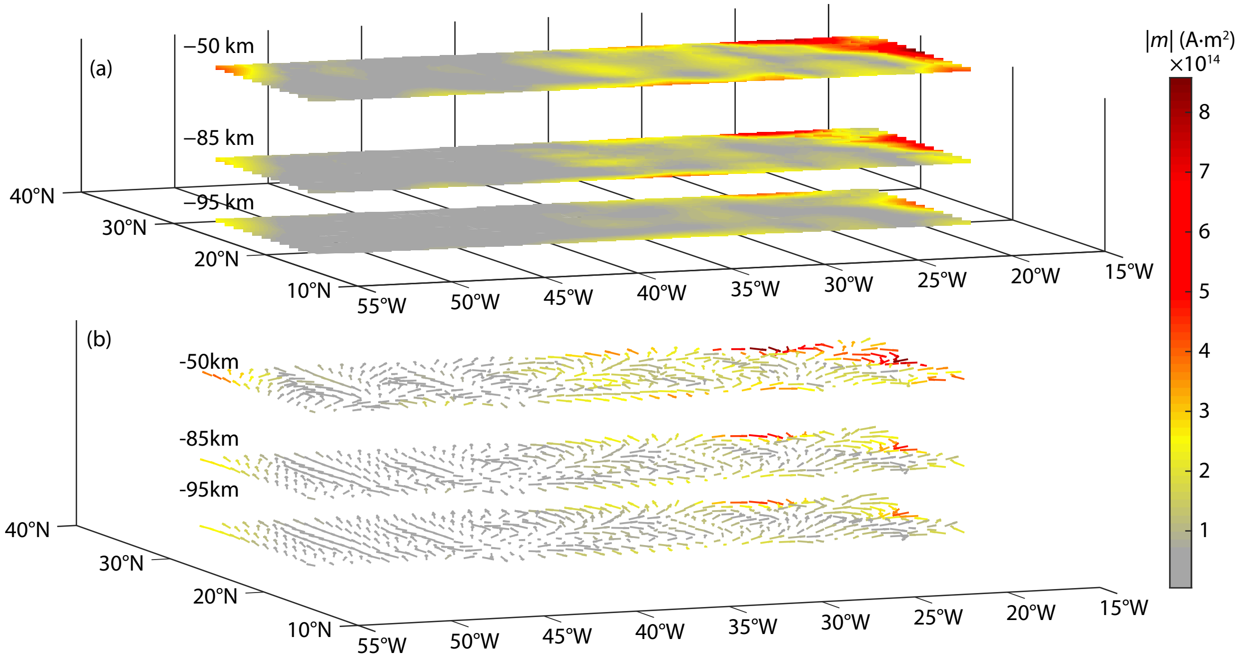

Figure 6. Distribution of the (a) strengths and (b) orientations of the inverted dipoles in each layer. The strength of the dipole moment is colored.

to the field data set of spacecraft. In the data set of L19, the spatial volume at the lower altitude (longitude 17°W–53°W, latitude 19°N–31°N, height 0–100 km) was partitioned into bins with a volume of 0.2° × 0.2° × 10 km (longitude × latitude × height). The magnetic fields at the center of these bins calculated by L19 constitute the field data set. We applied our model to this data set to invert the dipole moments at the three layers (the initial values for the dipoles were set as 1 A·m²). We then input the inverted dipoles as initial values to run our model again when subjected to the joint data set of the spacecraft. Finally, with the dipoles inverted in this way, we found the RMS of the model (not shown here), and the magnetic field pattern extrapolated to the surface of Mars did not change significantly (see Figure 7).

(3) The field components of some small-scale magnetic anomalies would attenuate quickly with height. Consequently, these components of the field could not be recorded significantly by the spacecraft at higher altitudes. It is unknown whether our model of the three-layer dipoles can infer these field components accurately on the surface of Mars with the data set from the spacecraft

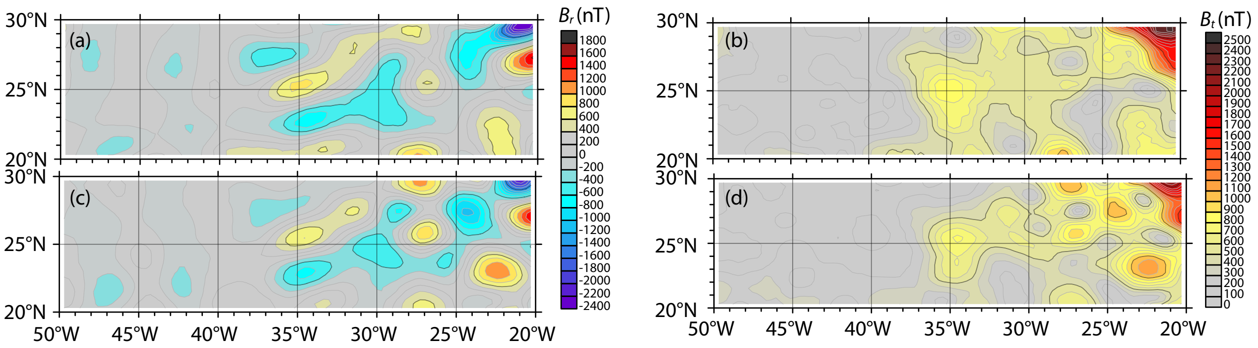

Figure 7. The upper panels show (a) the extrapolated radial magnetic field and (b) the magnetic field strength on the surface of Mars when the initial input values of the dipoles were set as 1 A·m^2. This is the same as shown in Figure 5. The lower panels show (c) the radial magnetic field and (d) the magnetic field strength when the initial values were calculated from the data set of L19 (the model by Langlais et al., 2019).

at high altitudes. Considering that the magnetometer onboard the InSight mission has so far provided unique magnetic field measurements on the surface of Mars (Johnson et al., 2020), we will check our model by comparison with the magnetometer data from InSight in the next study.

(4) We must mention that because of the inversion equivalence, the three-layer dipoles in our model may not reflect the actual pattern of the magnetic sources. It is necessary to explore other possible sources by combining our model with geological and geochemical studies in the future.

Acknowledgments

The magnetic field data from the MGS and MAVEN used in this paper are available from the Planetary Data System (http://ppi.pds.nasa.gov). This work was supported by the Strategic Priority Research Program of the Chinese Academy of Sciences (grant no. XDA17010201) and by the National Natural Science Foundation of China (grants nos. 41922031, 41774188, 41525016, and 41621063). We thank N. Q. Du and C. Zhang for constructive discussions.

Appendix A: The Conjugate Gradient Method

The conjugate gradient method is a classical method for solving symmetric positive definite linear equations. The idea of the conjugate gradient method is to find a pair of directions that are conjugate to each other according to the positive definite matrix, and then obtain the optimal solution along each conjugate direction.

The equation for the optimization problem can generally be written as follows:

$$\boldsymbol{b} = \boldsymbol{G}\boldsymbol{X} + \boldsymbol{v}, \tag{A1}$$

where $\boldsymbol{b}$ is a vector of the observation input, $\boldsymbol{G}$ is a transform matrix, $\boldsymbol{X}$ is a vector of the model parameters, and $\boldsymbol{v}$ is a vector of the random error.

Variable $\boldsymbol{G}$ may not be a positive definite matrix; thus, Equation (A1) can be transformed as follows:

$$\boldsymbol{G}^{\mathrm{T}}\boldsymbol{G}\boldsymbol{X} = \boldsymbol{G}^{\mathrm{T}}\boldsymbol{b}. \tag{A2}$$

If we take $Q = \boldsymbol{G}^{\mathrm{T}}\boldsymbol{G}$, $\boldsymbol{B} = \boldsymbol{G}^{\mathrm{T}}\boldsymbol{b}$, Equation (A2) can be rewritten as follows:

$$Q\boldsymbol{X} = \boldsymbol{B}. \tag{A3}$$

Thus, the task becomes finding an optimal solution, $\boldsymbol{X}^*$ of $\boldsymbol{X}$, to minimize $(Q\boldsymbol{X} - \boldsymbol{B})^{\mathrm{T}}(Q\boldsymbol{X} - \boldsymbol{B})$.

In the kth iteration of the conjugate gradient method, it needs to find direction $\boldsymbol{d}_k$ along which $\boldsymbol{y} = (Q\boldsymbol{X} - \boldsymbol{B})^{\mathrm{T}}(Q\boldsymbol{X} - \boldsymbol{B})$ decreases the fastest; it then needs to calculate the optimization step size α_k.

For the first iteration,

$$\boldsymbol{d}_0 = \boldsymbol{r}_0 = \boldsymbol{B} - Q\boldsymbol{X}_0, \tag{A4}$$

$$\alpha_0 = \frac{\boldsymbol{r}_0^{\mathrm{T}}\boldsymbol{r}_0}{\boldsymbol{d}_0^{\mathrm{T}}Q\boldsymbol{d}_0}, \tag{A5}$$

where $\boldsymbol{X}_0$ is the vector of initial values, α_0 is the initial step, and $\boldsymbol{r}_0$ is the vector of initial error.

For a subsequent kth iteration, the optimization direction should be conjugate orthogonal to any other optimization direction:

$$\boldsymbol{d}_k = \boldsymbol{r}_k + \frac{\boldsymbol{r}_k^{\mathrm{T}}\boldsymbol{r}_k}{\boldsymbol{r}_{k-1}^{\mathrm{T}}\boldsymbol{r}_{k-1}}\boldsymbol{d}_{k-1}, \tag{A6}$$

$$\boldsymbol{r}_k = \boldsymbol{B} - Q\boldsymbol{X}_k, \tag{A7}$$

where we have

$$\boldsymbol{X}_{k+1} = \boldsymbol{X}_k + \alpha_k\boldsymbol{d}_k, \tag{A8}$$

$$\alpha_k = \frac{\boldsymbol{d}_k^{\mathrm{T}}\boldsymbol{r}_k}{\boldsymbol{d}_k^{\mathrm{T}}Q\boldsymbol{d}_k}. \tag{A9}$$

References

Acuña, M. H., Connerney, J. E. P., Wasilewski, P., Lin, R. P., Anderson, K. A., Carlson, C. W., McFadden, J., Curtis, D. W., Mitchell, D., … Ness, N. F. (1998). Magnetic field and plasma observations at mars: initial results of the mars global surveyor mission. *Science*, *279*(5357), 1676–1680. https://doi.org/10.1126/science.279.5357.1676

Albee, A. L., Arvidson, R. E., Palluconi, F., and Thorpe, T. (2001). Overview of the Mars Global Surveyor mission. *J. Geophys. Res. Planets*, *106*(E10), 23291–23316. https://doi.org/10.1029/2000JE001306

Arkani-Hamed, J. (2005). Magnetic crust of Mars. *J. Geophys. Res. Planets*, *110*(E8), E08005. https://doi.org/10.1029/2004JE002397

Arkani-Hamed, J. (2007). Magnetization of Martian lower crust: Revisited. *J. Geophys. Res. Planets*, *112*(E5), E05008.

https://doi.org/10.1029/2006JE002824

Cain, J. C., Ferguson, B. B., and Mozzoni, D. (2003). An n = 90 internal potential function of the Martian crustal magnetic field. *J. Geophys. Res. Planets*, *108*(E2), 5008. https://doi.org/10.1029/2000JE001487

Chiao, L. Y., Lin, J. R., and Gung, Y. C. (2006). Crustal magnetization equivalent source model of Mars constructed from a hierarchical multiresolution inversion of the Mars Global Surveyor data. *J. Geophys. Res. Planets*, *111*(E12), E12010. https://doi.org/10.1029/2006JE002725

Connerney, J. E. P., Espley, J., Lawton, P., Murphy, S., Odom, J., Oliversen, R., and Sheppard, D. (2015). The MAVEN magnetic field investigation. *Space Sci. Rev.*, *195*(1), 257–291. https://doi.org/10.1007/s11214-015-0169-4

Fan, K., Fraenz, M., Wei, Y., Han, Q. Q., Dubinin, E., Cui, J., Chai, L. H., Rong, Z. J., Zhong, J., … Connerney, J. E. P. (2019). Reduced atmospheric ion escape above Martian crustal magnetic fields. *Geophys. Res. Lett.*, *46*(21), 11764–11772. https://doi.org/10.1029/2019GL084729

Geng, Y., Zhou, J. S., Li, S., Fu, Z. L., Meng, L. Z., Liu, J. J., and Wang, H. P. (2018). A brief introduction of the first mars exploration mission in China. *J. Deep Space Explor.* (*in Chinese*), *5*(5), 399–405. https://doi.org/10.15982/j.issn.2095-7777.2018.05.001

Han, X., Fraenz, M., Dubinin, E., Wei, Y., Andrews, D. J., Wan, W., He, M., Rong, Z. J., Chai, L., … Barabash, S. (2014). Discrepancy between ionopause and photoelectron boundary determined from Mars Express measurements. *Geophys. Res. Lett.*, *41*(23), 8221–8227. https://doi.org/10.1002/2014GL062287

Han, Q. Q., Fan, K., Cui, J., Wei, Y., Fraenz, M., Dubinin, E., Chai, L. H., Rong, Z. J., Wan, W. X., … Connerney, J. E. P. (2019). The relationship between photoelectron boundary and steep electron density gradient on Mars: MAVEN observations. *J. Geophys. Res.*: *Space Phys.*, *124*(10), 8015–8022. https://doi.org/10.1029/2019JA026739

Hestenes, M. R., and Stiefel, E. (1952). Methods of conjugate gradients for solving linear systems. *J. Res. Natl. Bur. Stand.*, *49*(6), 409–436. https://doi.org/10.6028/jres.049.044

Jakosky, B. M., Lin, R. P., Grebowsky, J. M., Luhmann, J. G., Mitchell, D. F., Beutelschies, G., Priser, T., Acuna, M., Andersson, L., … Zurek, R. (2015). The *Mars Atmosphere and Volatile Evolution* (MAVEN) mission. *Space Sci. Rev.*, *195*(1), 3–48. https://doi.org/10.1007/s11214-015-0139-x

Johnson, C. L., Mittelholz, A., Langlais, B., Lognonné, P., Pike, W. T., Joy, S. P., Russell, C. T., Yu, Y. N., Fillingim, M., … Banerdt, W. B. (2019). First results from the insight fluxgate magnetometer: Constraints on Mars' crustal magnetic field at the INSIGHT landing site. In *50th Lunar and Planetary Science Conference 2019*. The Woodlands, Texas: LPI.

Johnson, C. L., Mittelholz, A., Langlais, B., Russell, C. T., Ansan, V., Banfield, D., Chi, P. J., Fillingim, M. O., Forget, F., … Banerdt, W. B. (2020). Crustal and time-varying magnetic fields at the InSight landing site on Mars. *Nat. Geosci.*, *13*(3), 199–204. https://doi.org/10.1038/s41561-020-0537-x

Langlais, B., Purucker, M. E., and Mandea, M. (2004). Crustal magnetic field of Mars. *J. Geophys. Res. Planets*, *109*(E2), E02008. https://doi.org/10.1029/2003JE002048

Langlais, B., Thébault, E., Houliez, A., Purucker, M. E., and Lillis, R. J. (2019). A new model of the crustal magnetic field of Mars using MGS and MAVEN. *J. Geophys. Res. Planets*, *124*(6), 1542–1569. https://doi.org/10.1029/2018JE005854

Li, C. L., Liu, J. J., Geng, Y., Cao, J. B., Zhang, T. L., Fang, G. Y., Yang, J. F., Shu, R., Zou, Y. L.,... Ouyang, Z. Y. (2018). Scientific objectives and payload configuration of China's first Mars exploration mission. *J. Deep Space Explor.* (*in Chinese*), *5*(5), 406–413. https://doi.org/10.15982/j.issn.2095-7777.2018.05.002

Lillis, R. J., Frey, H. V., Manga, M., Mitchell, D. L., Lin, R. P., Acuña, M. H., and Bougher, S. W. (2008). An improved crustal magnetic field map of Mars from electron reflectometry: Highland volcano magmatic history and the end of the Martian dynamo. *Icarus*, *194*(2), 575–596. https://doi.org/10.1016/j.icarus.2007.09.032

Ma, Y. J., Fang, X. H., Russell, C. T., Nagy, A. F., Toth, G., Luhmann, J. G., Brain, D. A., and Dong, C. F. (2014). Effects of crustal field rotation on the solar wind plasma interaction with Mars. *Geophys. Res. Lett.*, *41*(19), 6563–6569. https://doi.org/10.1002/2014GL060785

Mayhew, M. A. (1979). Inversion of satellite magnetic anomaly data. *J. Geophys.*, *45*(2), 119–128.

Mittelholz, A., Johnson, C. L., and Morschhauser, A. (2018a). A new magnetic field activity proxy for Mars from MAVEN data. *Geophys. Res. Lett.*, *45*(12), 5899–5907. https://doi.org/10.1029/2018GL078425

Mittelholz, A., Morschhauser, A., Johnson, C. L., Langlais, B., Lillis, R. J., Vervelidou, F., and Weiss, B. P. (2018b). The Mars 2020 candidate landing sites: A magnetic field perspective. *Earth Space Sci.*, *5*(9), 410–424. https://doi.org/10.1029/2018EA000420

Moore, K. M., and Bloxham, J. (2017). The construction of sparse models of Mars's crustal magnetic field. *J. Geophys. Res. Planets*, *122*(7), 1443–1457. https://doi.org/10.1002/2016JE005238

Morschhauser, A., Lesur, V., and Grott, M. (2014). A spherical harmonic model of the lithospheric magnetic field of Mars. *J. Geophys. Res. Planets*, *119*(6), 1162–1188. https://doi.org/10.1002/2013JE004555

Mustard, J., Adler, M., Allwood, A., Bass, D., Beaty, D., Bell, J., et al. (2013). Report of the Mars 2020 science definition team. Mars Exploration Program Analysis Group (MEPAG), Cl, 155-205. http://mepag.jpl.nasa.gov/reports/MEP/Mars_2020_SDT_Report_Appendix.pdf

Němec, F., Morgan, D. D., Gurnett, D. A., and Brain, D. A. (2011). Areas of enhanced ionization in the deep nightside ionosphere of Mars. *J. Geophys. Res. Planets*, *116*(E6), E06006. https://doi.org/10.1029/2011JE003804

Oliveira, J. S., Langlais, B., Pais, M. A., and Amit, H. (2015). A modified Equivalent Source Dipole method to model partially distributed magnetic field measurements, with application to Mercury. *J. Geophys. Res. Planets*, *120*(6), 1075–1094. https://doi.org/10.1002/2014JE004734

Plattner, A., and Simons, F. J. (2015). High-resolution local magnetic field models for the Martian South Pole from Mars Global Surveyor data. *J. Geophys. Res. Planets*, *120*(9), 1543–1566. https://doi.org/10.1002/2015JE004869

Purucker, M., Ravat, D., Frey, H., Voorhies, C., Sabaka, T., and Acuña, M. (2000). An altitude-normalized magnetic map of Mars and its interpretation. *Geophys. Res. Lett.*, *27*(16), 2449–2452. https://doi.org/10.1029/2000GL000072

Purucker, M. E., Sabaka, T. J., and Langel, R. A. (1996). Conjugate gradient analysis: A new tool for studying satellite magnetic data sets. *Geophys. Res. Lett.*, *23*(5), 507–510. https://doi.org/10.1029/96gl00388

Purucker, M. E. (2008). A global model of the internal magnetic field of the Moon based on Lunar Prospector magnetometer observations. *Icarus*, *197*(1), 19–23. https://doi.org/10.1016/j.icarus.2008.03.016

Russell, C. T., Joy, S., Yu, Y., Rowe, K., Johnson, C., Mittelholz, A., Langlais, B., Chi, P. J., Fillingim, M., …Banerdt, B. (2019). The insight magnetic field measurements: preliminary results. In *50th Lunar and Planetary Science Conference 2019*. The Woodlands, Texas: LPI.

Smith, D. E., and Zuber, M. T. (2002). The crustal thickness of Mars: Accuracy and resolution. In *33rd Annual Lunar and Planetary Science Conference*. Houston, Texas: NASA.

Trotignon, J. G., Mazelle, C., Bertucci, C., and Acuña, M. H. (2006). Martian shock and magnetic pile-up boundary positions and shapes determined from the Phobos 2 and Mars Global Surveyor data sets. *Planet. Space Sci.*, *54*(4), 357–369. https://doi.org/10.1016/j.pss.2006.01.003

Wei, Y., Yao, Z. H., and Wan, W. X. (2018). China's roadmap for planetary exploration. *Nat. Astron.*, *2*(5), 346–348. https://doi.org/10.1038/s41550-018-0456-6

Whaler, K. A., and Purucker, M. E. (2005). A spatially continuous magnetization model for Mars. *J. Geophys. Res. Planets*, *110*(E9), E09001. https://doi.org/10.1029/2004JE002393

Zhao, L., Du, A. M., Qiao, D. H., Sun, S. Q., Zhang, Y., Ou, J. M., Guo, Z. F., Li, Z., Feng, X., … Li, F. (2018). The ROVER fluxgate magnetometer. *J. Deep Space Explor.* (*in Chinese*), *5*(5), 472–477. https://doi.org/10.15982/j.issn.2095-7777.2018.05.010

Zuber, M. T. (2001). The crust and mantle of Mars. *Nature*, *412*(6843), 220–227. https://doi.org/10.1038/35084163